CASL-U-2014-0208-000

Power uprates
and plant life extension

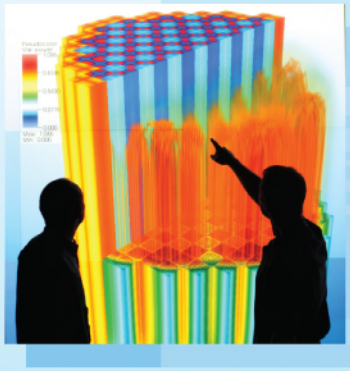

Engineering design
and analysis

Science-enabling
high performance
computing

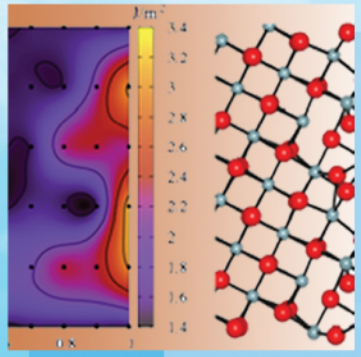

Fundamental science

Plant operational data

Consortium for Advanced Simulation of LWRs

L3:THM.CLS.P9.02

Transient Evolution and Dispersion of Bubbles in a Channel and Data Mining

Jiacai Lu and Gretar Tryggvason
University of Note Dame

September 30, 2014

U.S. DEPARTMENT OF ENERGY | Nuclear Energy

CASL-U-2014-0208-000

Transient Evolution and Dispersion of Bubbles in a Channel and Data Mining

L3:THM.CLS.P9.02 milestone report

Jiacai Lu
Gretar Tryggvason

University of Notre Dame

September 30, 2014 (Ver. 1.1)

CASL-U-2014-0208-000

Abstract: The transient motion of bubbles in vertical channels is studied using direct numerical simulations. A simulation of a large number of bubbles of different sizes at a friction Reynolds number of 500 shows that small bubbles quickly migrate to the wall, but the flow takes much longer to adjust to the new bubble distribution. The simulation has provided a large database that is currently being examined to both obtain overall average quantities as well as filtered values for comparison with LES results. Simulations of much smaller laminar systems with several spherical bubbles have been used to examine the full transient toward steady state and those show a non-monotonic evolution where all the bubbles first move toward the walls and then the flow slowly slows down, eventually allowing some bubbles to return to the center of the channel. Several simulations have also been done to understand the limiting case of bubbly flow with zero gravity. Those generally show a uniform bubble distribution and relatively minor modifications of the flow, compared to a single-phase flow. Finally, a few simulations have been done for flow regime changes, when bubbles coalesce. Those are still very preliminary but open up the possibility of much more extensive examination of high void fraction flows.

One of the main conclusions from these studies is that while the rearrangement of bubbles takes place relatively quickly, the time needed for the bubbles to have significant effect on the flow is much longer. This suggests that understanding the transient evolution of the flow in response to a change in the bubble distribution is particularly important.

Contents

LIST OF FIGURES *4*

LIST OF TABLES *5*

1. RELEVANCE TO CASL AND OBJECTIVES *6*

2. COMPUTATIONAL SETUP *6*

3. RESULTS *6*

3.1 Transient evolution of a large number of bubbles 6

3.2 Zero buoyancy bubbles in turbulent flows 19

3.3 The transient motion of bubbles in a laminar channel flow 22

3.4 High volume fraction flow with regime change 27

4. FUTURE WORK *31*

REFERENCES *32*

APPENDIX: DESCRIPTION OF THE NUMERICAL CODE *33*

List of Figures

Figure 0. Computational domain and setup.

Figure 1. Bubbles in the large run at times 4, 34 and 64.

Figure 2. The bubbles and the vorticity at times 4, 34 and 64, using λ_2=-2.

Figure 3. Vortices are visualized by the iso-surface of λ_2=-2 at time 34. Here red indicates a positive streamwise component and blue a negative one. Light blue, green and yellow are horizontal vortices.

Figure 4. Close up of the vortical structures at time=64. On the left we show vorticity next to the left wall (using λ_2=-2) and on the right we show vorticity in the interior of the domain (using λ_2=-4).

Figure 5. The mean streamwise liquid velocity across the channel at different times.

Figure 6. The Reynolds stresses (normalized by $(u^+)^2$, where u^+ is the friction velocity) across the channel at different time steps.

Figure 7. The void fraction at three different times, along with the predictions of a simple model for the void fraction at steady state.

Figure 8. The streamwise vorticity squared (normalized by $1/t_0^2$, where t_0 is a reference time equal to μ/τ_w) across the channel at different time steps.

Figure 9. The streamwise velocity fluctuations (normalized by u^+, where u^+ is the friction velocity) across the channel at different time steps.

Figure 10. The wall-normal velocity fluctuations (normalized by u^+, where u^+ is the friction velocity) across the channel at different time step.

Figure 11. Horizontal flow rate of bubbles (Fb) across the channel at different time steps

Figure 12. Turbulent Kinetic Energy (normalized by $(u^+)^2$) across the channel.

Figure 13. Dissipation Rate (normalized by $(u^+)^4/\nu$) across the channel.

Figure 14. The wall shear stress and the liquid flow rate versus time.

Figure 15. The original flow field and the flow field after applying a box filter that is slightly larger than the diameter of the smallest bubbles. λ_2=-2 on the left and $\lambda_{2=}$-1 on the right.

Figure 16. The average velocity, the void fraction and the turbulent kinetic energy versus the spanwise coordinate at time 64, for two different filter sizes. The results for the original unfiltered field is also shown.

Figure 17. A comparison of the filtered Reynolds stress term <uv> and the product of the filtered velocities <u><v> as computed at several sample point in the liquid at time 34.

Figure 18. One frame from a simulation of bubbles in a turbulent channel when gravity is turned off. iso-

surface of λ_2=-0.75

Figure 19. The average streamwise velocity (top), the void fraction (middle) and the Reynolds stresses (bottom) for simulations with 48 bubbles of different sizes.

Figure 20. The bubble distribution at several different times (0, 10, 20, 48, 98, and 176), starting with the initial condition in the upper left corner.

Figure 21. The average liquid velocity (top), the void fraction profile (middle), and the Reynolds stresses (bottom) at the same times as shown in figure 20.

Figure 22. The wall shear stress (top) and the liquid flow rate (bottom) versus time for the run in figures 20 and 21.

Figure 23. The transition from bubbly flow to slug flow in a vertical channel, for relatively high void fraction.

Figure 24. Two frames from a simulation of the evolution of low surface tension bubbles into a slug.

Figure 25. The average velocity of the mixture versus time for three runs with different surface tension (top) and the projection of the surface area in the streamwise direction versus time.

Figure 26. The wall shear (top) and the projection of the surface area in the streamwise direction versus time for two different coalescence criteria.

List of Tables

Table I. The distribution of bubble sizes for the large run described in this section. The bubble diameter is in computational units.

1. Relevance to CASL and Objectives

Development and validation of closure laws for computational multiphase fluid dynamics (CMFD) is a necessary part of successful prediction of reactor thermal hydraulics behavior. The objective of the presented study is to complement experimental data by providing both the physical insight and the quantitative data needed for the development of new and advanced closure laws.

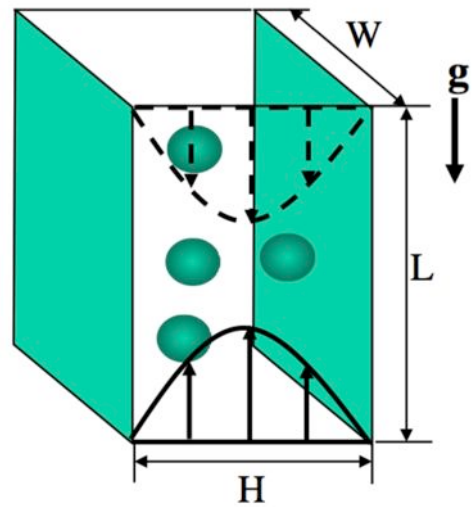

Figure 0. Computational domain and setup.

2. Computational Setup

The computations are done using the FTC3D code briefly described in the appendix. The computational domain is a rectangular channel, bounded by two rigid vertical walls, and periodic in the streamwise and the spanwise direction. The initial flow field and the location of the bubbles is give. For initially turbulent flows we have checked that evolving the flow field in time without the bubbles preserves the character of the flow and that the average turbulent statistics is constant. The grid is uniform in the streamwise and spanwise direction, but in the wall-normal direction it is stretched to give a finer resolution near the walls. The computational domain is shown in figure 1.

3. Results

The focus of our studies this year has been on the transient evolution of many bubble systems. We have examined several systems and although the computational setup is the same, the purpose of each set of simulations has been somewhat different. We start by discussing a simulation started last year, and continued this year, of a large system.

3.1 Transient evolution of a large number of bubbles

The first set of results has been obtained for a system where amny bubbles interact with turbulent flow and other bubbles of different sizes. This is the largest system that we have examined so far and has been run using 2048 processors on the Titan. Last year we discussed preliminary results for a relatively short time.

The domain size is $2\pi \times 4 \times \pi$ in the streamwise, wall normal and spanwise direction, respectively, resolved by $1024 \times 768 \times 512$ grid points. The physical parameters are selected such that the Morton number is equal to 5.75×10^{-10} and the void fraction is 0.0304. The bubbles come in four sizes, as listed in Table I. The majority of the bubbles are small and we expect the smallest two sets of bubbles to accumulate at the wall, since our earlier results suggest that the transition between bubbles pushed to the wall and those that are not is around Eo=2.5. The numbers of bubbles for each group were selected

so that there are enough small bubbles that can be pushed to the wall to put the core in hydrostatic equilibrium. The properties of the fluid and the bubbles are the same as in our earlier simulations, but the domain size is eight times larger, giving a friction Reynolds number of Re^+ =500. The bubbles are initially distributed nearly uniformly across the domain but as they start to rise, the smaller bubbles start to migrate toward the walls and form a dense wall-layer. For channels with spherical bubbles, where the lift force pushes the bubbles toward the wall and a bubbly wall-layer is formed, it can be shown that the steady state consists of a wall-layer and a homogeneous core region where the number of bubbles is such that the weight of the mixture balances the imposed pressure gradient. Thus, if the overall void fraction is given, the void fraction in both the core and the wall-layer can be found. In figure 1 we show the bubbles at three times. The first frame is just after the simulations started, at time 4 (in computational units), the second frame is at time 34 and the last frame is at time 64. In the second frame many of the small bubbles have moved to the wall, but the there are still several small bubbles in the middle, along with most of the larger bubbles. This evolution continues in the third frame, and more of the smallest bubbles are now at the wall, along with a large fraction of the bubbles from the next larger group. In figure 2 we show the vorticity (and the bubbles) using the λ_2 method to visualize the vorticity. It is clear that the vorticity is increased initially as the bubbles start to move. The vortical structures in the first figure correspond roughly to what we would expect in a single-phase flow, since the initial velocity is taken to be single-phase turbulent flow. In the second frame the bubbles have added considerable vorticity in the interior of the domain, while the wall vorticity has not been modified significantly. In the third frame a clear center region has, however, started to appear, with fewer bubbles and less vortical structures than in the middle frame. To understand the vortical structure a little better, we show the vorticity in figure 3, again visualized by the λ_2 method but now coloring the vortical structures according to their orientation. Thus, both red and blue vortical structures are aligned with the flow, but red have a positive rotation while the blue ones have a negative rotation. The intermediate colors (light blue, green and yellow) indicate vortical structures that are not aligned with the flow. As expected, the majority of the vortical structures aligned with the flow come in pairs, such that a blue structure is frequently found next to a red one. We have examined the vorticity for several times, including varying the iso-contour value for λ_2, and in figure 4 we show a close up of the vorticity for two regions of the flow at time 64. On the left we show the vorticity next to the left wall (using λ_2=-2) and on the right we look at the vorticity in the interior, now using λ_2=-4, so the vorticity appears more concentrated and low levels of vorticity are not visible. The figure shows that the longitudinal vortices that one expect in turbulent boundary layers do appear to survive the addition of the bubbles to the wall-layer, at least at the time plotted here, and suggests that vorticity shed by the large bubbles is responsible for the majority of the vorticity in the interior of the channel. Vortices that are mostly horizontal do, for the most part, encircle bubbles.

Number of Bubbles	Diameter of Bubbles	Eotvos Number
4	0.4414	3.805
13	0.3856	2.904
50	0.306	1.829
504	0.16	0.50

Table I. The distribution of bubble sizes for the large run described in this section. The bubble diameter is in computational units.

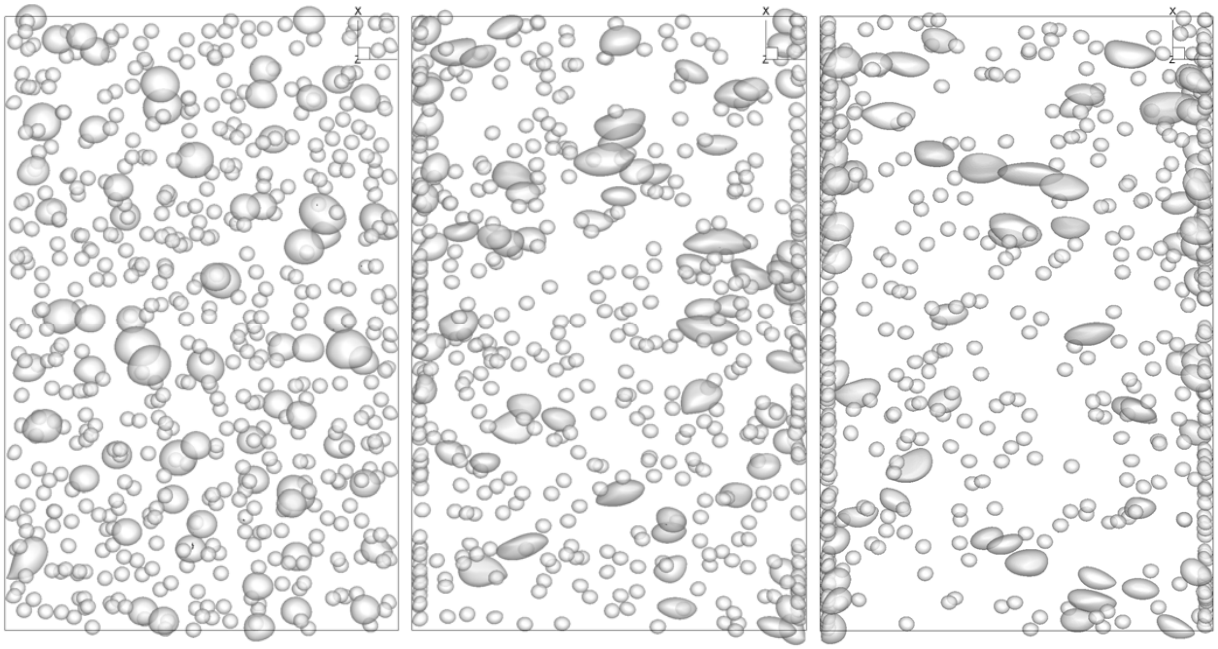

Figure 1. Bubbles in the large run at times 4, 34 and 64.

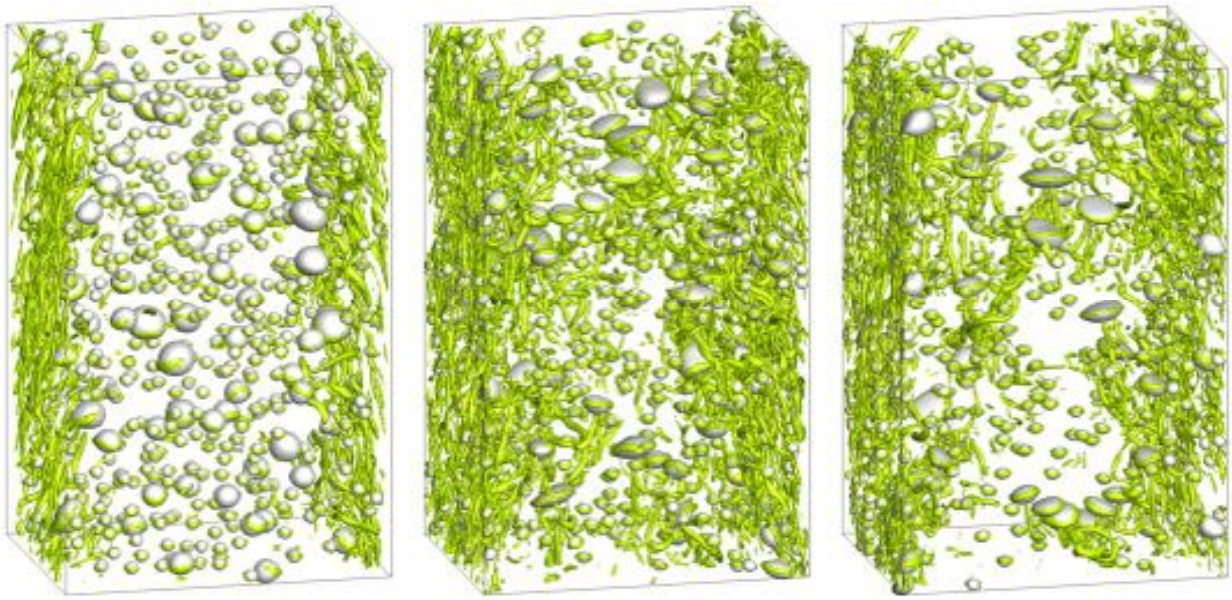

Figure 2. The bubbles and the vorticity at times 4, 34 and 64, using λ_2=-2.

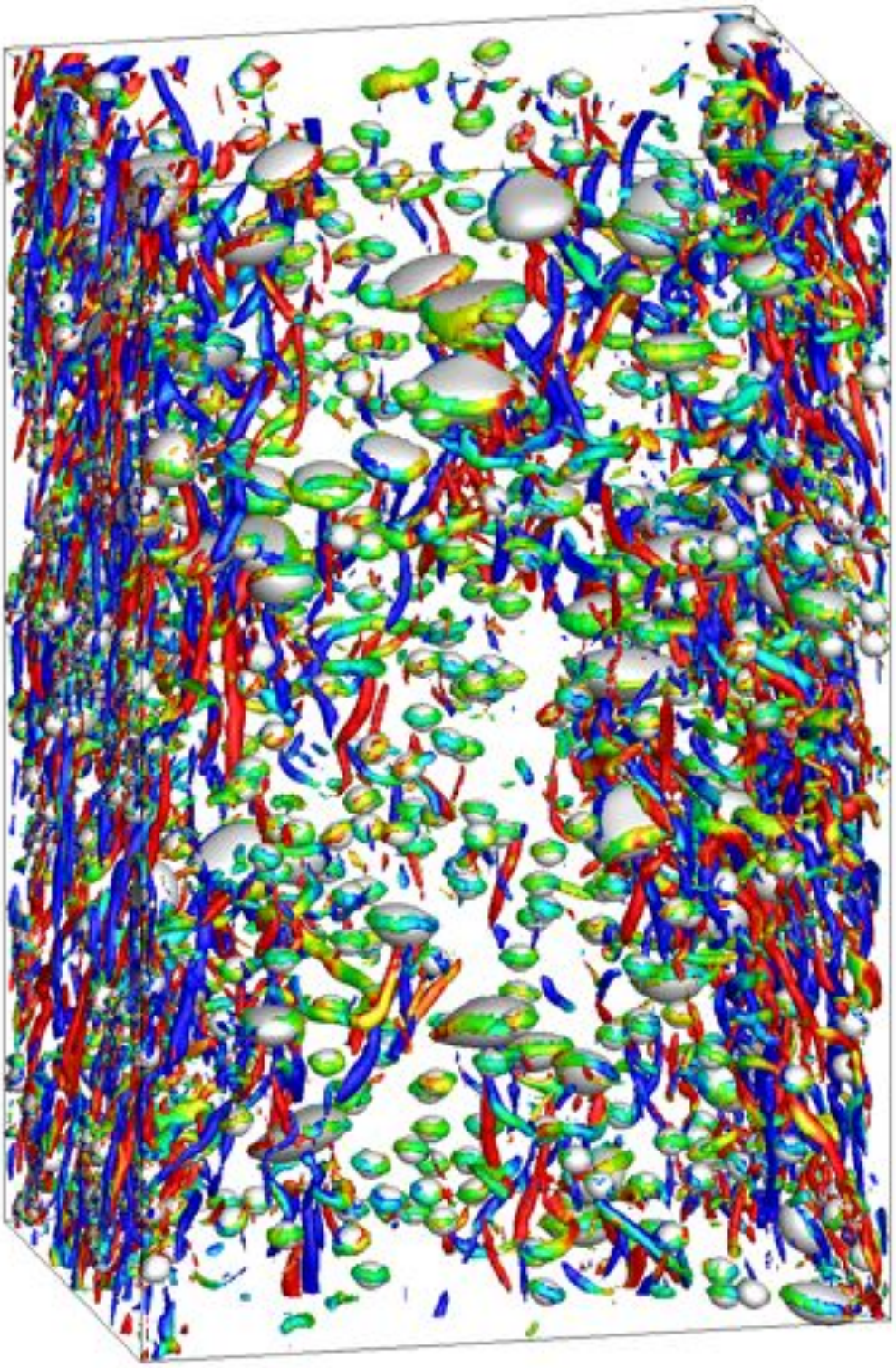

Figure 3. Bubbles and vortices visualized by the iso-surface of λ_2=-2, at time 34. Here red indicates a positive streamwise component and blue a negative one. Light blue, green and yellow are horizontal

vortices.

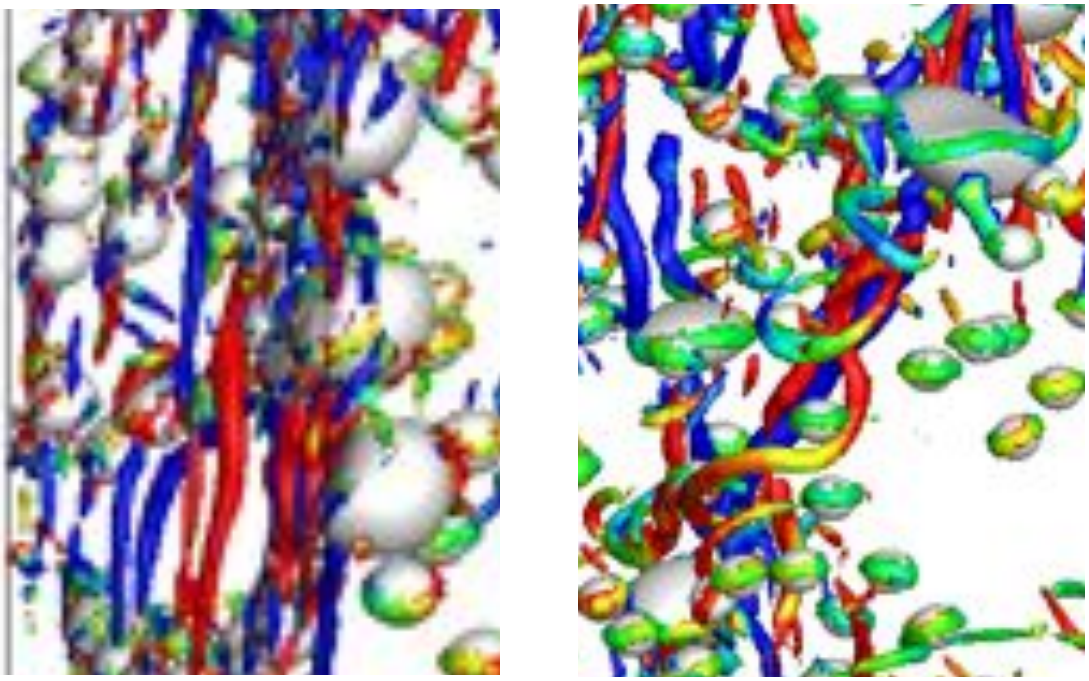

Figure 4. Close up of the vortical structures at time=64. On the left we show vorticity next to the left wall (using λ_2=-2) and on the right we show vorticity in the interior of the domain (using λ_2=-4).

In figures 5 to 13 we show several quantities averaged over planes parallel to the walls, versus the horizontal coordinate at three times (4, 34, and 64, all in computational units). We showed some of the same quantities in the last report, but only for the earlier times.

The average streamwise velocity is plotted in figure 5 and it is clear here that the average velocity has not changed much, so far. This is expected since the small bubbles must first move to the wall to form a layer there before the presence of the layer starts to influence the velocity. As the flow evolves further, however, we expect the presence of the bubbles at the wall to reduce the flow rate. Experience with bubbles in turbulent upflow at smaller Reynolds numbers and in smaller laminar systems (see section 3.3), suggest that this will take significant time.

The modest modification of the flow due to the presence of the bubbles at the early times is also seen in figure 6, where the turbulent shear <u'v'> is plotted versus the horizontal coordinate. At steady state <u'v'> should go to zero in the middle of the channel, if the evolution is the same as we have seen for smaller systems. The average profile has not changed much at time 34, and shows the linear shape expected for a single-phase flow, but at time 64 it has leveled off slightly, indicating that flow is starting to change.

Figure 7 shows that while the average velocity has not changed much, the void fraction has. The black dashed line is the predictions of the simple model for the void fraction at steady state originally presented in our earlier work. Initially the bubbles are relatively uniformly distributed but as the bubbles

start to move upward the small bubbles start to migrate toward the wall. This leads to an increase in the void fraction there and at the latest time the distribution has almost reached the steady state value. We note, however, that the results discussed later in the report suggest that the convergence to steady-state may not be monotonic.

The average streamwise vorticity squared is plotted in figure 8. We see that the vorticity in the center of the channel increases slightly, as the bubbles start to move and generate vorticity, and that the structure of the vorticity near the wall starts to change. At the earliest time we see the vorticty distribution we expect for a single phase flow, that is a peak close to the wall corresponding to hairpin vorticies and then a maximum right at the wall corresponding to the wall bound vorticity needed to bring the velocity to zero. When the bubbles move toward the wall this changes and we see a significant increase in the vorticty near the wall. The peak near the wall due to the hairpin vortices is also no longer as clearly visible.

The change in the velocity fluctuations is explored in the next two figures where we plot the streamwise velocity fluctuations (figure 9) and the wall-normal velocity fluctuations (figure 10), versus the horizontal coordinate. As expected the presence of the bubbles initially increases the velocity fluctuations in the middle of the channel and the wall-normal fluctuations near the wall. However, as more bubbles move to the walls, the velocity fluctuations in the center seem to slightly decrease again.

In figure 11 the flux of bubbles across the channel is plotted at the two later times. Negative values mean that the bubbles are going to the left and positive values indicate motion to the right. The bubble flux fluctuates strongly but it is clear that at the earlier time the flux is mostly negative on the left side and positive on the right hand side, clearly indicating a flux of bubbles to the wall. The very large fluctuations seen at both times, however, suggest that we need to examine the fluxes separately for different size bubbles.

For turbulence modeling we need the turbulent kinetic energy, figure 12, and the dissipation rate, figure 13. The turbulent kinetic energy increases slightly as the bubbles start to modify the flow, both near the walls as well as in the middle of the channel, but at this time the distribution has not changed in any fundamental way. The dissipation rate shows a similar structure as the streamwise vorticity squared and increases both near the walls and in the middle of the channel.

As the void fraction distribution in figure 7 shows most clearly, the flow is evolving and given the steady state results for smaller systems and lower Reynolds numbers we expect its structure to continue to change. To get some insight into how far the system is away from steady state, we plot the flow rate of the liquid and the wall shear stress versus time, in figure 14. At steady state the wall shear simply balances the weight of the mixture plus the pressure gradient so it is known and given by the dashed line. Clearly, we are far away from steady state. The initial conditions are set up such that wall shear balanced the weight and the pressure gradient, but as the bubbles move to the wall, they increase the wall-shear and the flow must therefore decelerate as is seen in the liquid flow rate. Eventually the shear rate will start to decrease again and asymptotically approach the dashed line. We note, however, that

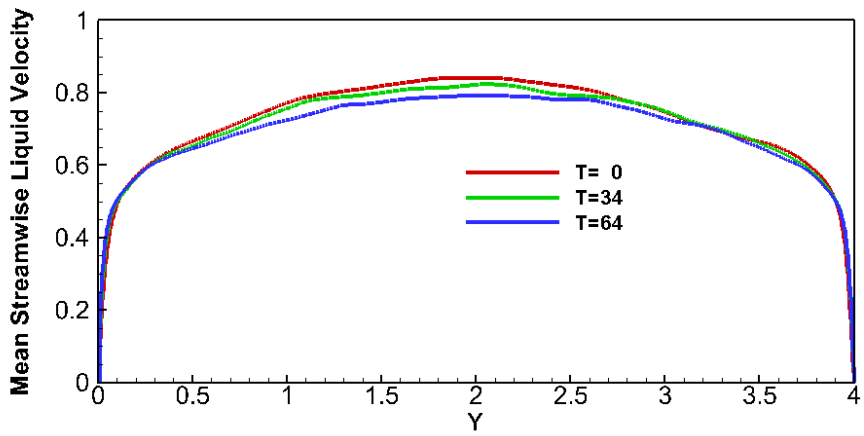

Figure 5. The mean streamwise liquid velocity across the channel at different times.

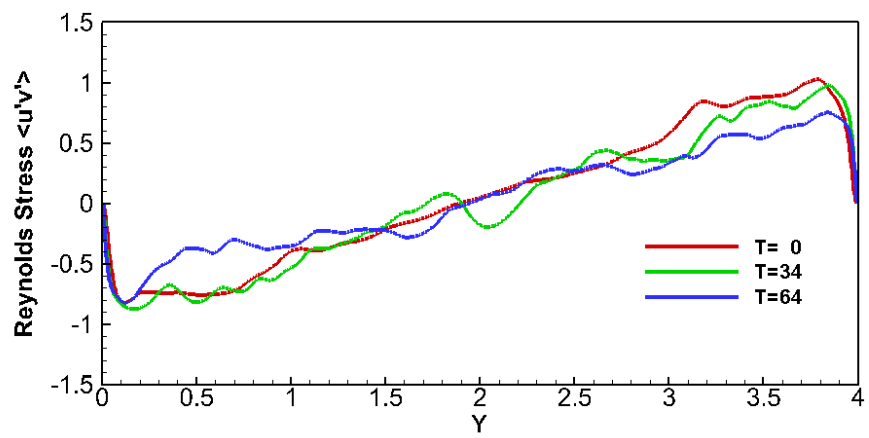

Figure 6. The Reynolds stresses (normalized by $(u^+)^2$, where u^+ is the friction velocity) across the channel at different times.

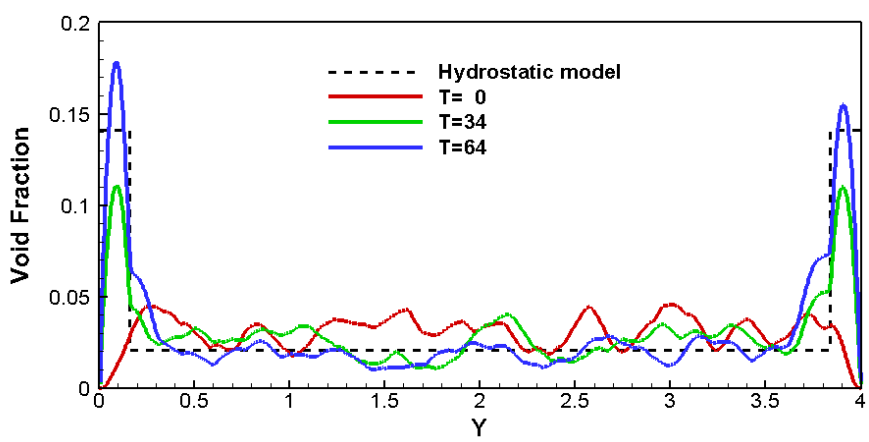

Figure 7. The void fraction at three different times, along with the predictions of a simple model for the void fraction at steady state.

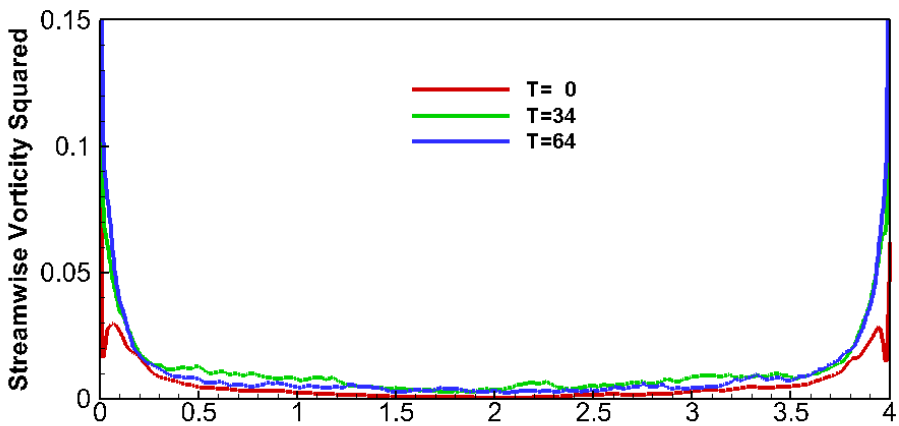

Figure 8. The streamwise vorticity squared (normalized by $1/t_0^2$, where t_0 is a reference time equal to μ/τ_w) across the channel at different times.

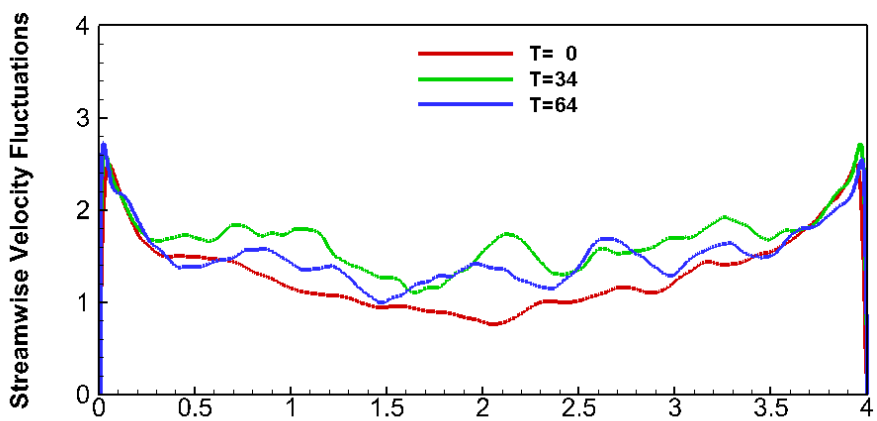

Figure 9. The streamwise velocity fluctuations (normalized by u^+, where u^+ is the friction velocity) across the channel at different times.

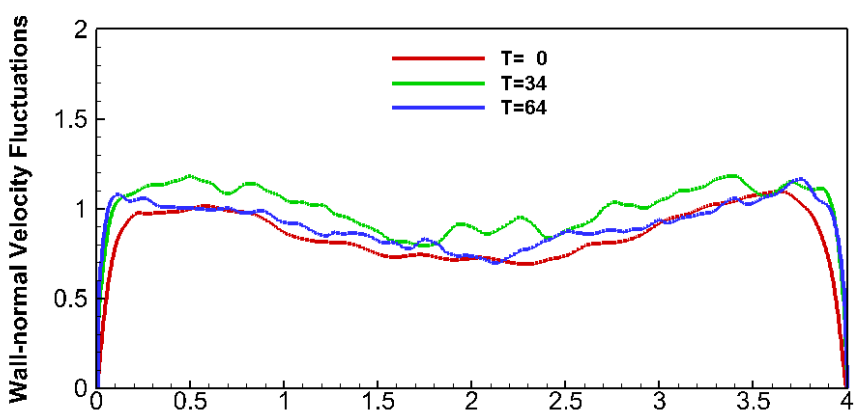

Figure 10. The wall-normal velocity fluctuations (normalized by u^+, where u^+ is the friction velocity) across the channel at different times.

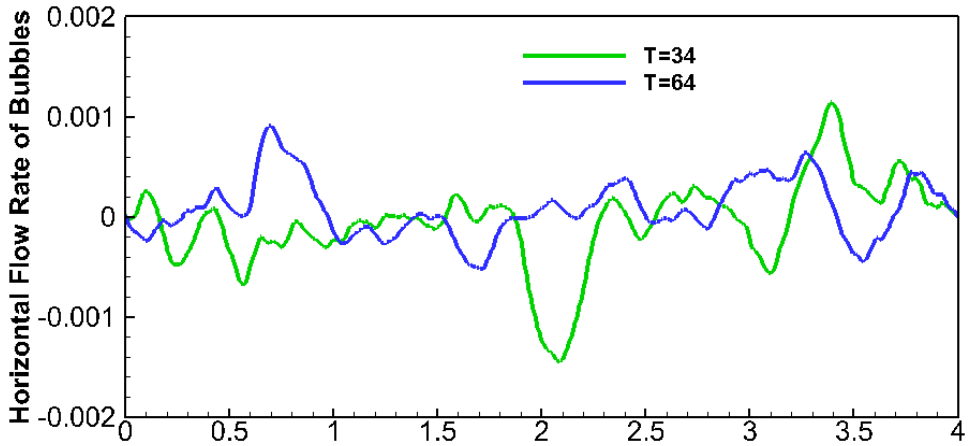

Figure 11. Horizontal flow rate of bubbles (Fb) across the channel at different times.

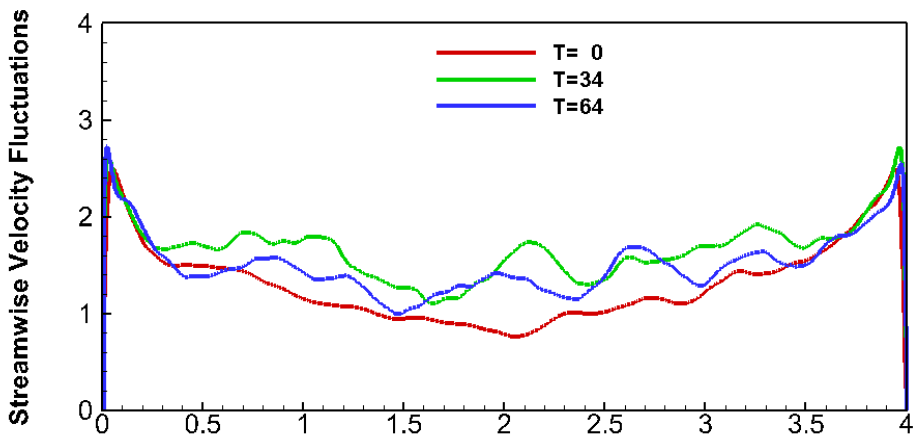

Figure 12. Turbulent Kinetic Energy (normalized by $(u^+)^2$) across the channel.

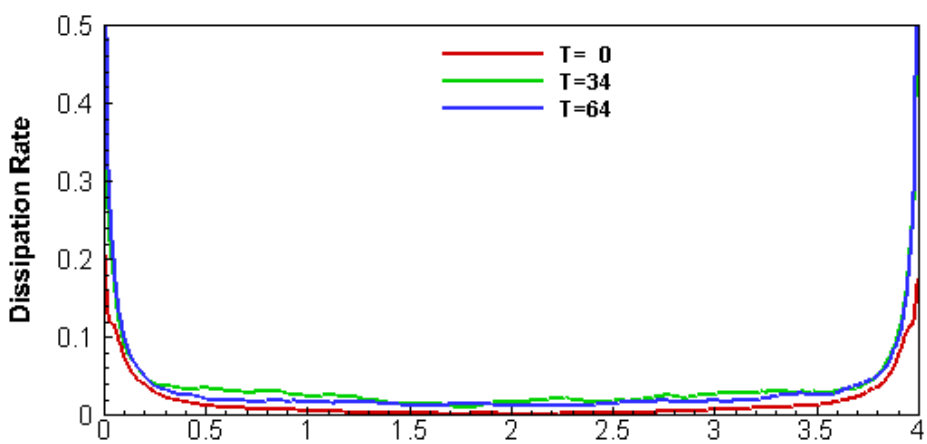

Figure 13. Dissipation Rate (normalized by $(u^+)^4/\nu$) across the channel.

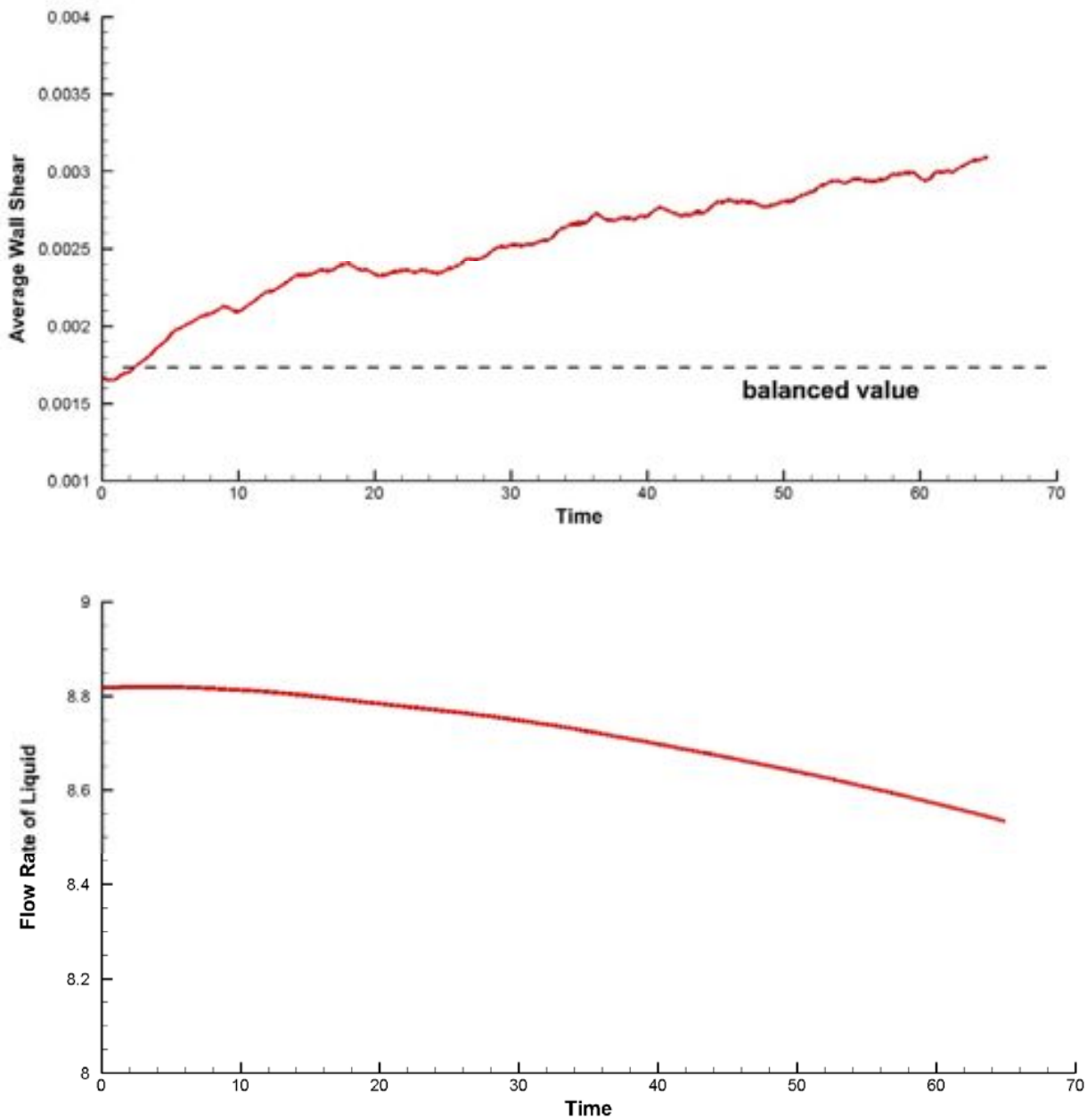

Figure 14. The wall shear stress and the liquid flow rate versus time. The dashed line shows the steady state wall shear.

some aspects, such as the average velocity, has not changed much for the time examined here. This suggest that care must be exercised when interpreting short time results for turbulent bubbly flows since the results may appear to be at steady state whereas they actually are still evolving but on a relatively long timescale. Furthermore, the results suggest that it is important to follow the evolution for a longer time to capture fully the modification that the bubbles have on the flow.

So far, we have focused on the average properties of the flow and how they evolve. Increasingly,

however, as computer power increases, there is an interest in modeling multiphase flows using LES. The standard approach to LES is to filter the Navier-Stokes equations to derive equations for the large scale and we have started to use the database described above to explore the structure of the filtered fields. For other work on filtering of the Navier-Stokes equations for multiphase flows, see Labourasse et al. 2007, Toutant et al. 2007 & 2009; Vincent et al. 2008; Trontin et al. 2010; and Jamet et al. 2010.

We have started examining filtered fields but using a simple box filter, defined by

$$G_\Delta(\mathbf{x}) = \begin{cases} 1 \; if \; |\mathbf{x}| < \Delta \\ 0 \; if \; |\mathbf{x}| > \Delta \end{cases}$$

and applying it to both the velocity field and the interface:

$$\bar{\mathbf{u}}(\mathbf{x}) = \int G_\Delta(\mathbf{x}-\mathbf{x}')\mathbf{u}(\mathbf{x}')d\mathbf{x} \qquad \text{and} \qquad \bar{\mathbf{X}}(s) = \int G_\Delta(\mathbf{X}(s)-\mathbf{X}(s'))\mathbf{X}(s')ds',$$

where the bar denotes the filtered quantity. Notice that here we apply the filter separately to the velocity field and the interface. We could, of course, also have applied the filter to the indicator function (as Toutant et al. 2008, do) but then bubbles smaller than the filter size disappear, instead of collapsing to a point particle, as happens in the present approach. We do believe that the different filtering approaches are related and that one can be explicitly related to the other, but we have not done so yet.

Applying the filtering to the flow field and the interface results in smoother flow. In figure 15 we show a small part of the domain at time 34, before we apply the filter (left frame) and after we apply the filter (right frame). The filter size is slightly larger than the smallest bubbles so those collapse to point particles (for plotting purpose we give them a finite size), the larger bubbles become rounder and the maximum vorticity is reduced. As noted in the figure caption, we use a different value for the iso-contours of λ_2 in the different frames to allow us to better see the vortical structures.

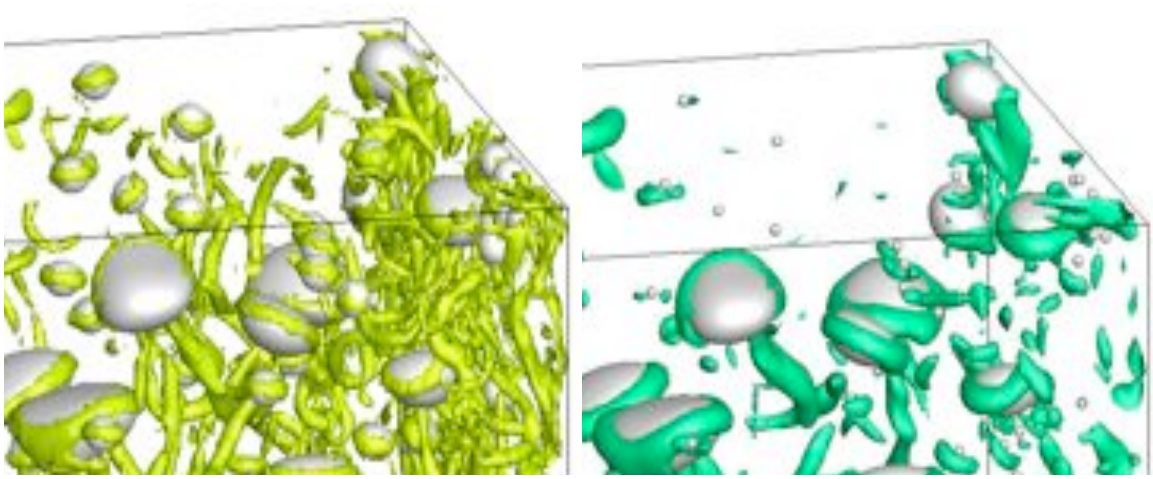

Figure 15. The original flow field and the flow field after applying a box filter that is slightly larger than the diameter of the smallest bubbles. λ_2=-2 on the left and λ_2=-1 on the right.

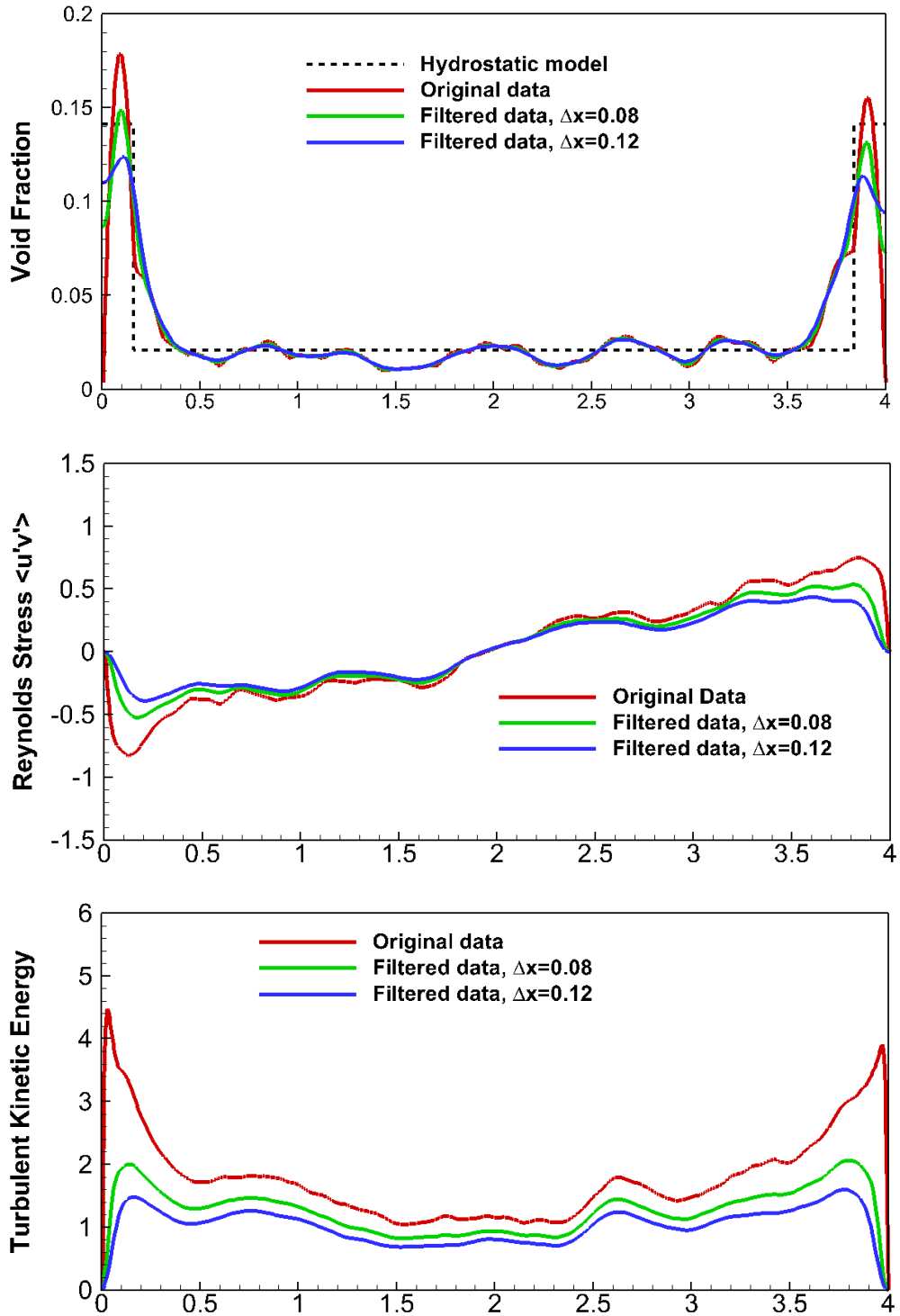

Figure 16. The void fraction, the Reynolds stresses and the turbulent kinetic energy versus the spanwise coordinate at time 64, for two different filter sizes. The results for the original unfiltered field are also shown.

We have applied different size filters to the flow field and in figure 16 we show the effect of the filter size on the void fraction, the Reynolds stresses and the turbulent kinetic energy at time 64. The filter size has modest effect on the void fraction and very little on the average velocity field (not shown). It does, however, obviously have some effects of the average of the fluctuating or turbulent quantities.

While the effect of the filtering on the averaged quantities is important, of more interest is how the filtered quantities relate to the unfiltered flow. We have only recently started to examine the relationship of the filtered quantities to the unfiltered ones, and only show a couple of preliminary examples here. In figure 17 we compare different filtered terms---using <> to denote filtered quantities---by sampling the domain and plotting two differently filtered terms as a pair of points in a scatter plot. In (a) we plot the product of the density and two filtered velocity components versus the filtered product of the original quantities or <ρ<u><v>> versus <ρuv> and see that while those quantities are clearly not equal (not falling on the 45 degree line) the relationship is fairly linear. In (b) we plot the difference between two terms versus the difference between two other terms, or <ρ<u><v>> - <ρ><<u><v>> versus <ρuv> - <ρ><u><v>, and again the points are off the 45 degree line but the relationship is nearly linear. In the limit of small filter size we expect the filtering to have very little effects and while filter size is fairly small here (equal to the size of the smallest bubbles) it is clearly big enough to make a difference. Toutant et al. (2008) found similar results in their `a priory' tests of LES models for two-fluid flows. Both plots are based on sampling a relatively small part of the domain and we expect these results to be modified as we explore the whole domain and other times.

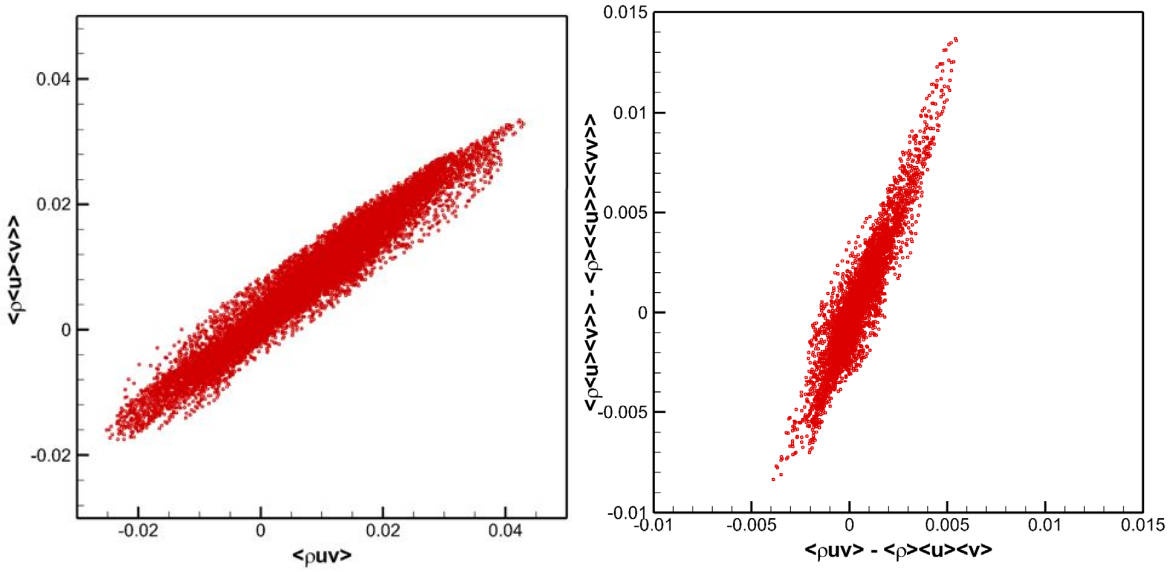

Figure 17. (a) A comparison of <ρ<u><v>> versus <ρuv> at several sample points at time 34. (b) A comparison of or <ρ<u><v>> - <ρ><<u><v>> versus <ρuv> - <ρ><u><v>, at several sample points at time 34.

3.2 Zero buoyancy bubbles in turbulent flows

The void fraction profile in vertical bubbly flow is the result of lateral motion of the bubbles. The lateral motion is determined by the lift on each bubble and possibly by turbulent dispersion. In studies of drag reduction in turbulent flows it has been found that the dispersion quickly removes bubbles injected near the walls (thus reducing their effect on the drag) and thus dispersion may have some effect on the void fraction distribution, particularly for high Reynolds numbers and low slip velocities.

We have done several simulations of bubbles in turbulent channel flows where we have turned gravity off, so the slip velocity is zero. While this is a limiting case, unlikely to be encountered in a fuel assembly, we hope that it gives us some insight into the bubble distribution in the absence of buoyancy effects.

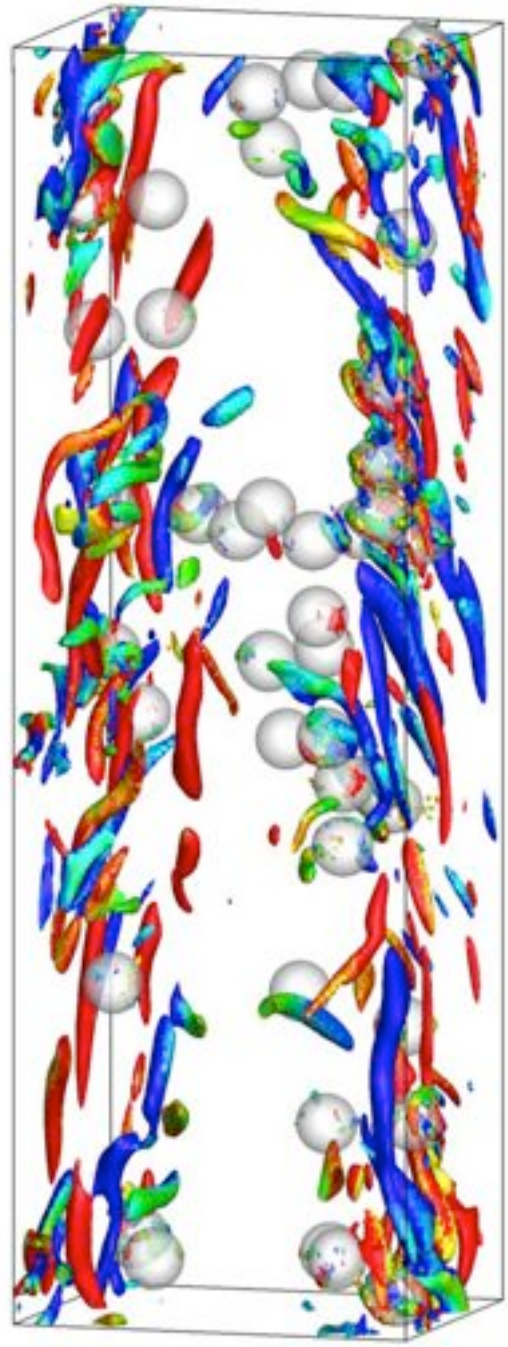

Figure 18. One frame from a simulation of bubbles in a turbulent channel when gravity is turned off. Iso-surface of λ_2=-0.75

Figure 18 shows one frame from a simulation of 42 bubbles with a diameter of 0.2 in turbulent flow. The vorticity is visualized as in figure 3, but the value for the iso-surface of λ_2=-0.75. The Reynolds number here is much lower than in the large run (Friction Reynolds Number Re+=150), so the number and intensity of the vortices is much lower. The vortical structures are similar to what is seen for single phase flows and there are no horizontal vortices encircling the bubbles, since the slip velocity is essentially zero. We have simulated several cases to study the effect of the bubble size and the void fraction, but only include a few sample results here, all computed after the flow has reached an approximate steady state. In figure 19 (a) we show the average velocity profile versus the spanwise coordinate for single-phase flow and bubbles of different size. Here we keep the number of bubbles fixed so the void fraction changes as well. As we expect, the addition of the bubbles has relatively minor effect on the average velocity, particularly for the smallest bubbles (and lowest void fraction). For larger bubbles and higher void

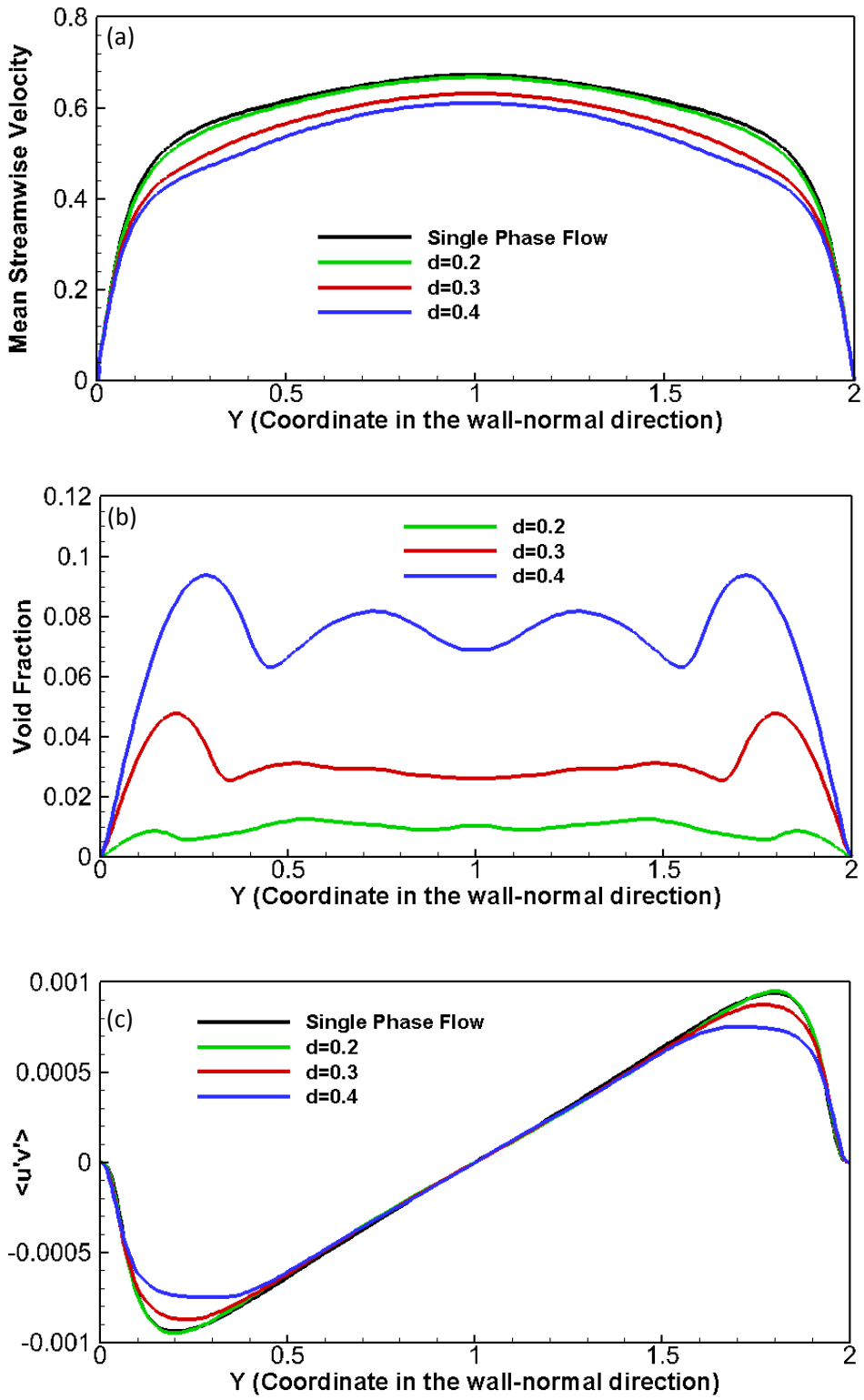

Figure 19. The average streamwise velocity (top), the void fraction (middle) and the Reynolds stresses (bottom) for simulations with 48 bubbles of different sizes.

fraction we see some reduction but the shape of the velocity profile remains similar to the single phase flow. The plot of the average void fraction versus the horizontal coordinate, figure 19(b), shows that for all three bubble sizes the void fraction is relatively uniform in the middle of the channel, but that there is a slight “bump” near the walls for the larger bubbles. An inspection of the bubble distribution for those cases shows that some bubbles slide along the walls, but that they usually do so transiently and eventually are carried away by the turbulence. The increase in the void fraction does, however, modify the various fluctuating quantities and in figure 19(c), where we show the Reynolds stresses versus the horizontal coordinate, it is clear that while the data for the smallest bubbles is essentially identical to the single phase flow, the values are reduced for the larger bubbles in exactly the same region as we saw an increase in void fraction. Similar results are found for other measures of the velocity fluctuations.

Other simulations where we vary the void fraction and the bubble diameter suggest that the flow modification is a stronger function of the size of the bubbles, rather than the void fraction, at least for the parameter ranges examined so far.

Although the addition of large bubbles reduces the total flow rate slightly, the relatively modes modification of the single phase flow generally leads to relatively fast convergence to the new flow configuration, unlike the very long transient required for buoyant flows.

3.3 The transient motion of bubbles in a laminar channel flow

While the main focus of our work this year has been on turbulent flows, earlier studies have shown that often there is considerable similarity with results from laminar flows and since such simulations are generally much easier, starting with a laminar flow allows us to explore the dynamics for a longer time more easily then for when we start with turbulent flow. In our earlier studies of the steady state we found that reaching a state, where the average flow rate and void fraction distribution are approximately fixed, took a long time and we therefore used various “short-cuts” to accelerate the evolution as mush as possible.

The transient evolution is important for several reasons. First of all, it is relatively long so in practical applications it is likely that it is encountered frequently and possibly more often than the steady state, and secondly, the relatively simple structure of the flow at steady state is not very sensitive to the various parameters in models of the average flow evaluation. The void fraction distribution does, for example, only depend on the sign of the bubble lift coefficient but not its magnitude. To understand how bubbly flow evolves toward a steady state we have conducted several simulations of the evolution of bubbly flows, starting with bubbles placed randomly in a parabolic laminar velocity field.

Figure 20 shows the bubbles and the velocity field in a mid-plane through the domain at several times. The first frame is at time zero where the flow is parabolic and the bubbles are spread nearly uniformly across the channel. In the next frame (at time 10) the bubbles have started to accumulate near the walls and in the third frame (at time 20) most of the bubbles have moved toward the wall. There is a well-defined layer of bubbles right at the wall (clearer on the left wall, although other figures at different times show a similar layer on the right wall) and a cluster of bubbles next to it. The bubble motion is fairly unsteady and the wall-layer is often broken up by the motion of the bubbles just outside of it. This development continues in the fourth frame (time 48), where the middle of the channel is mostly free of bubbles and the bubbles on the right wall form two fairly compact layers, but on the left wall the distribution is more irregular. In the fifth frame, however, all the bubbles are at the walls, where they form fairly compact layers. In the sixth frame, at a much later time (time 176), several bubbles have moved back to the middle of the channel and the wall-layers consists of only one layer of bubbles.

The overall evolution of the flow is also seen in figure 21 where we plot the average liquid velocity (top), the void fraction profile (middle), and the shear rate (bottom) at the same times as shown in figure 20. The initially parabolic velocity decreases rapidly in the middle of the channel but increases initially near the walls. At the last time the velocity is nearly uniform across almost the whole channel, going to zero only very near the walls. The void fraction profile is more complex but a careful inspection shows that the bubbles rapidly accumulate near the walls, with the void fraction going to zero in the middle of the channel and then returning to a profile consisting of nearly uniform value across most of the channel with peaks near the walls, representing a layer of thickness of about one bubble diameter. Similar evolution is seen for the shear rate profile, which is initially linear across the channel as in laminar

single-phase flow and then gradually transitions to zero in the middle of the channel and large spikes near the wall.

Another way of looking at the unsteady evolution of the flow is shown in figure 22 where we plot the average wall-shear (top) and the average flow rate (bottom). The initial conditions are such that the wall-shear balances the weight of the mixture and the imposed pressure gradient, but as bubbles are pushed to the wall the wall-shear increases and decelerates the flow, as seen in the results for the large turbulent flow. Between times 10 and 20 the wall-shear however reaches a maximum and then gradually decreases and approaches the expected steady state value very slowly. The wall-shear curve is fairly irregular since the wall-shear changes rapidly when bubbles move toward and away from the wall. The average flow rate is much smoother and the flow slows down monotonically, in agreement with figure 21.

It is clear from these figures that when nearly spherical bubbles are injected into parabolic flow the evolution toward steady state is highly non-monotonic. First all the bubbles migrate towards the walls leaving the center region nearly free of bubbles. Then the presence of the bubbles near the wall increases the shear there and reduces the flow rate. As the flow rate is reduced some of the bubbles migrate back into the core region until the mixture there is in hydrostatic equilibrium. The initial migration of the bubbles to the wall takes place relatively fast, but the slowing down of the flow and the migration of the bubbles back into the core is a much slower process. Here we do not allow the bubbles to coalesce, but if they could then the migration to the wall might promote the formation of either larger bubbles that would move away from the wall relatively quickly or possibly a gas film at the wall.

We have done a few simulations using the same governing parameters but different initial bubble locations and confirmed that the overall evolution is similar in all cases and that the time scale is also comparable.

The transient data described above has also been used in preliminary work on exploring the use of data mining techniques to extract closure laws from multiphase DNS data. Although this work is relatively exploratory and funded by the National Science Foundation and not CASL, it is of obvious relevance to CASL and if successful it is likely to influence modeling in a significant way. Thus, we are including a short discussion here. The main idea is that the DNS results contain a detailed description of the flow, both spatially and temporally so that the closure terms in the averaged equations can be calculated at every spatial and temporal location. Everything else is also known about the flow and we can similarly compute the average velocity, void fraction, and any other quantity of interest. The fundamental assumption behind modeling the average flow is that the closure terms appearing in the model equations depend on the average flow and possibly some integral measures of the unresolved motion, such as the turbulent kinetic energy and dissipation rate and area density. For turbulent flows it is essential to include integral measures of the unresolved motion but here we assume that such terms are not needed, since all the unsteadiness is due to the motion of the bubbles. Thus, closing the equations requires us to find a relation that gives the closure terms as functions of the averaged quantitates

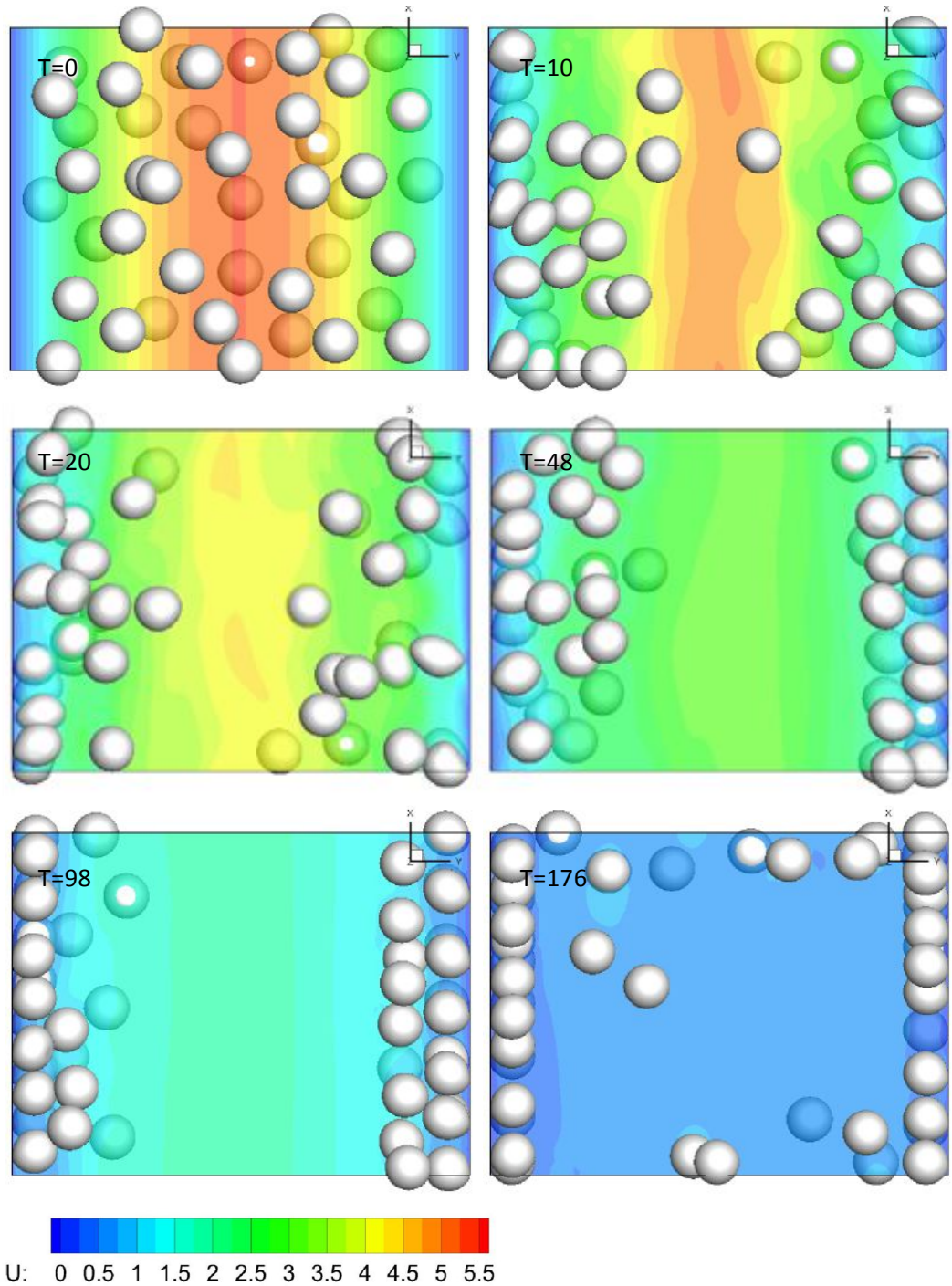

Figure 20. The bubble distribution at several different times (0, 10, 20, 48, 98, and 176), starting with the initial condition in the upper left corner. The color is the streamwise velocity and it is clear that the flow is slowing down with time.

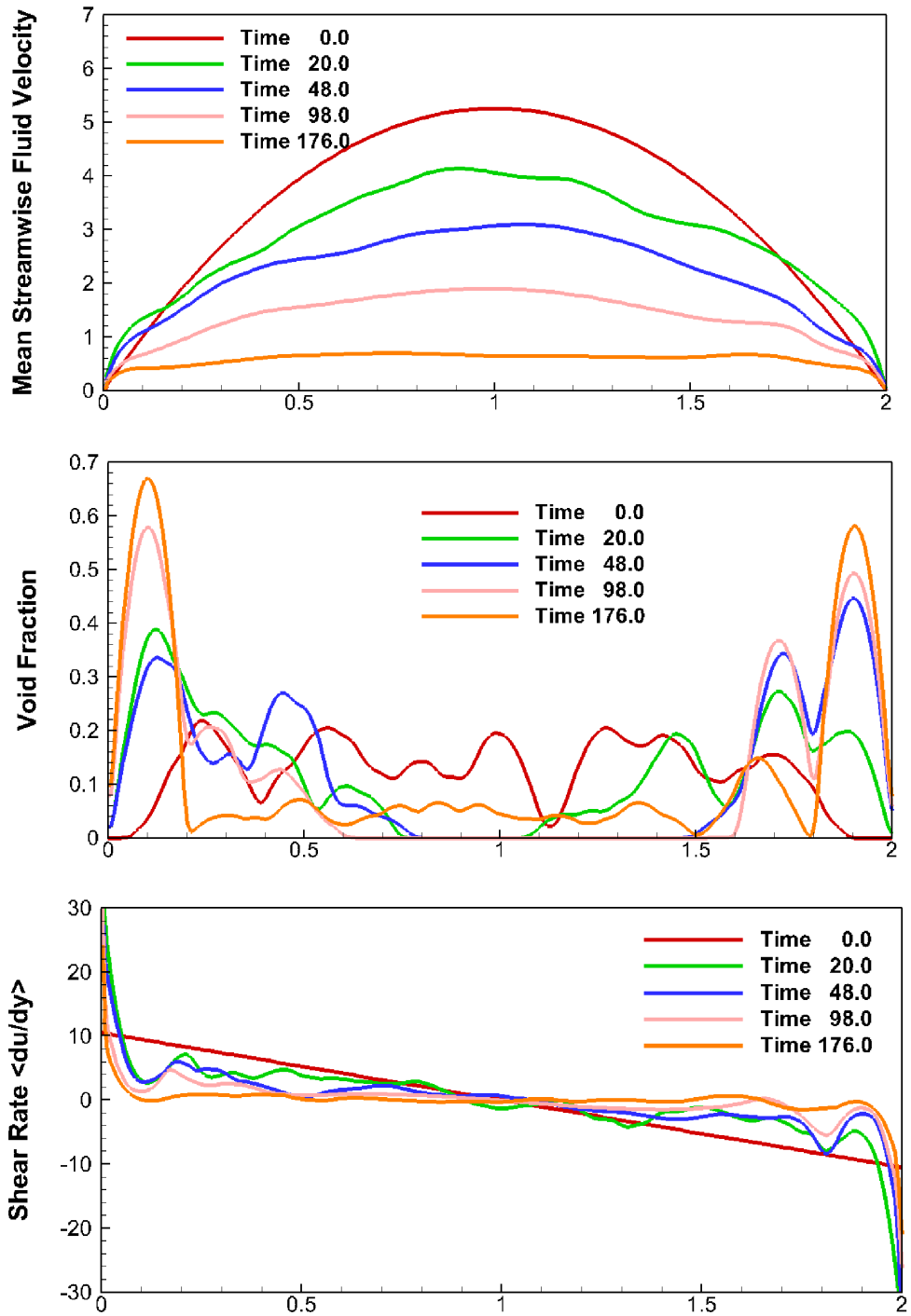

Figure 21. The average liquid velocity (top), the void fraction profile (middle), and the shear rate (bottom) at the same times as shown in figure 20.

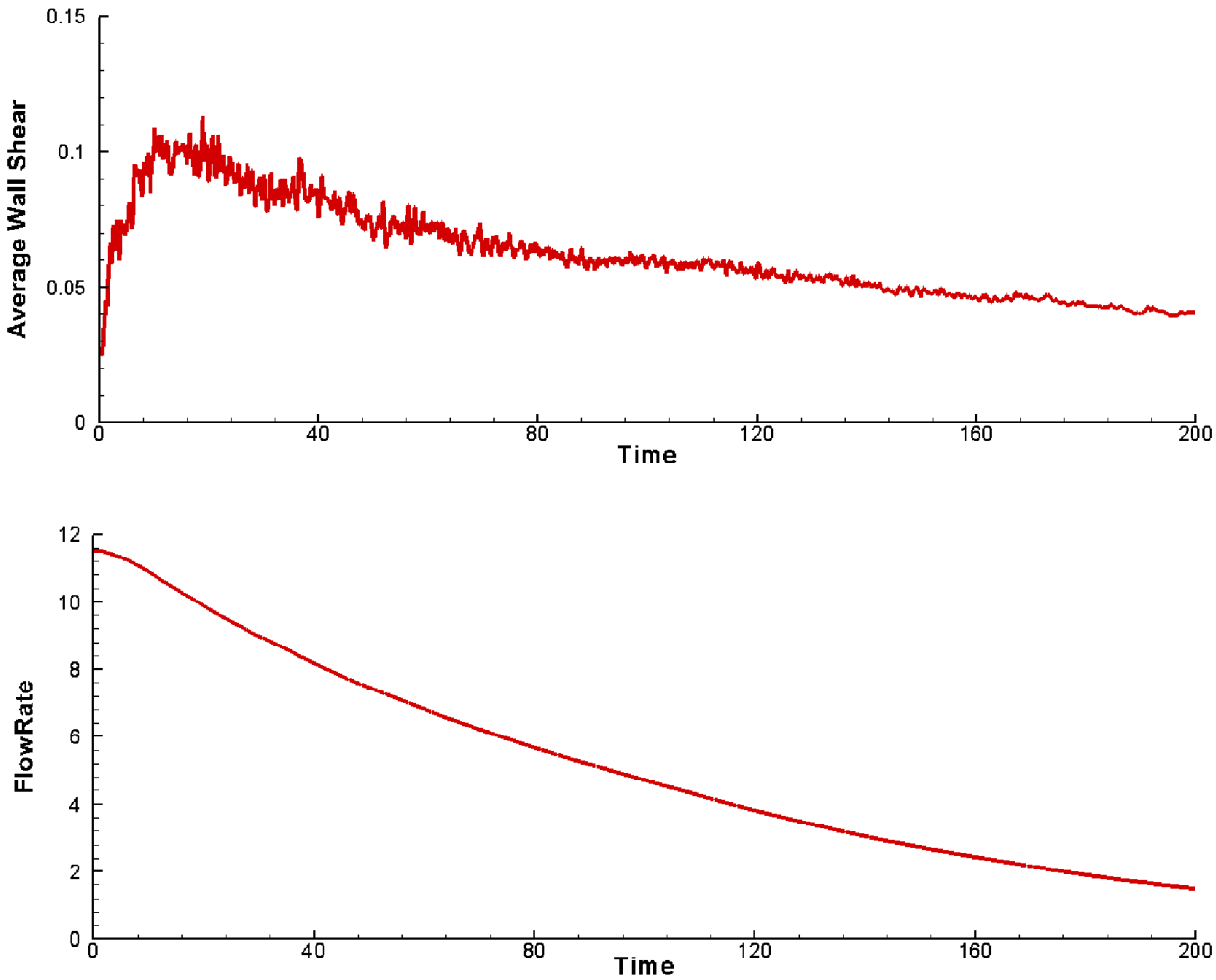

Figure 22. The wall shear stress (top) and the liquid flow rate (bottom) versus time for the run in figures 20 and 21.

appearing in the model equations, or derivatives of the averages quantities. Efforts to find these relationships have a long history and in most cases the functional of the relationship is proposed, with parameters that are then determined from experimental data. Here we are exploring a more general approach and use Neural Networks to determine the relationship. We have also used regression, where we assume that the relationship is given by a linear combination of the various independent quantities and multiplies of those. The results obtained so far are promising, particularly for the evolution of the void fraction away from walls, but questions about how to prepare the data and account for the large fluctuations seen in the data, as well as how to capture the evolution at the wall more accurately are still under investigation.

3.4 Preliminary Results for High Volume Fraction Flow with Regime Change

Bubbly flows are a natural starting place for efforts to model multiphase flows, since the interfaces are relatively well defined. However, in many cases, particularly if the void fraction is high, the interface topology is much more complex and the interfaces undergo continuous coalescence and breakup. Modeling such flows is still very primitive and we expect DNS to be able to cast considerable light on the various processes governing the flow. Topology changes in multiphase flows take place through two primary mechanisms: films that rupture and threads that break. DNS must be able to accurately handle both. For methods that track the indicator function identifying the different fluids or phases directly on an Eularian grid (such as VOF or Level Set methods), topology change will take place when the resolution of a film or a thread is sufficiently low, whereas methods that use connected marker points to track the interface will generally not allow a change in topology. Both methods can be modified to either allow or prevent topology changes, but at the cost of additional code and possibly increased runtime. Of the two types of topology changes, thin threads that break are by far the easier to deal with. The Navier-Stokes equations predict that the diameter of threads can become zero in a finite time and no additional physical modeling needs to be included. Furthermore, the breakup is fast, so while there may be a moment just before the thread breaks when it is not well resolved, this is often such a short time that it does not have a significant effect on the overall dynamics of the flow. Both types of methods generally handle thread breakup easily, with marker point methods leaving an inert string of particles behind. The rupture of thin films is a much more complex matter. The thickness of a draining film, simulated using the standard Navier-Stokes equations, does usually not become zero in a finite time and it is only because of the presence of short range attractive forces that it eventually becomes unstable and holes are formed. The initial hole is then usually enlarged by either the formation of other holes that merge with the first one or the enlargement of the original hole by rim breakup that includes the formation of drops with threads that snap, but often on such a small scale that it is difficult to resolve them fully in simulations focusing on a larger region of the flow. The rupture of films in simulations using numerical methods that track the indicator function directly is an artifact of the finite resolution and in some cases it is found that refining the grid postpones the rupture and prevents the solution from converging to a grid independent form. While in many cases such methods produce methods that look “physical,” it is not well understood when the rupture is adequately controlled artificially by the resolution and when more complete rupture models must be included. When the interface is tracked by connected marker points it is necessary to add a strategy to rupture the interfaces when they are close enough but this results in a complete control of when, or under what circumstances, rupture takes place, thus allowing us to examine how sensitive the overall evolution of the flow is to how the rupture takes place, even if a complete rupture model is not included.

We have started to explore the dynamics of flows undergoing topology changes by doing a few simulations of the transition from bubbly flows to slug flow---so far working only with laminar flows. This transition takes place mostly through the rupture of thin films, as the bubbles coalesce, although bubble breakup and the breaking of thin threads is also seen. We have a topology change algorithm that seems to work well for both mechanisms, although a slight extension is needed to extend thread breakup for

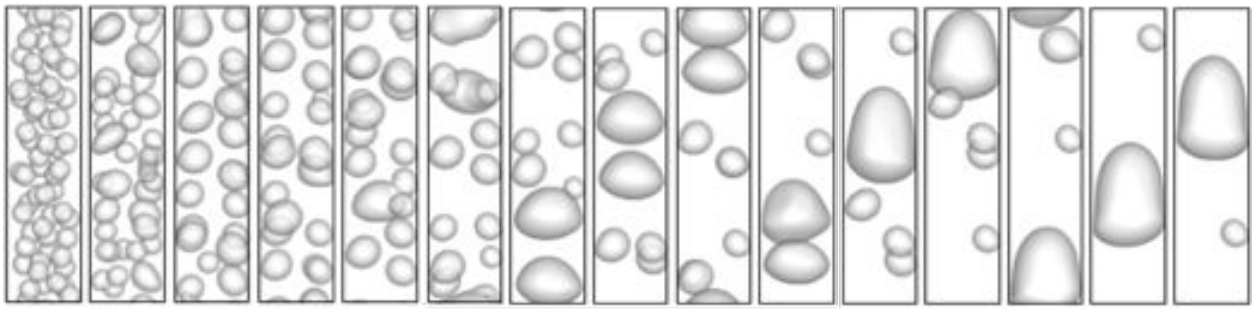

Figure 23. The transition from bubbly flow to slug flow in a vertical channel, for relatively high void fraction. Time goes from left to right.

periodic domains. We note that although the topology change algorithm was developed several years ago is has not been published yet.

Figure 23 shows results from one simulation of the coalescence of several bubbles in a channel flow into a large slug. The simulation is done using a grid with 320 by 80 by 80 grid points and thin films are ruptured if they become thinner than one grid spacing, thus making the results similar to what we would expect from a VOF or Level Set computation. The first frame shows the bubbles, as placed in an initially parabolic flow, and subsequent frames show the bubbles gradually becoming larger and fewer, until in the last frame we see one large slug and only one small bubble. In this case the void fraction is 21% and the initial number of bubbles is sixty. The surface tension is selected such that the initial Eötvös number is 0.45.

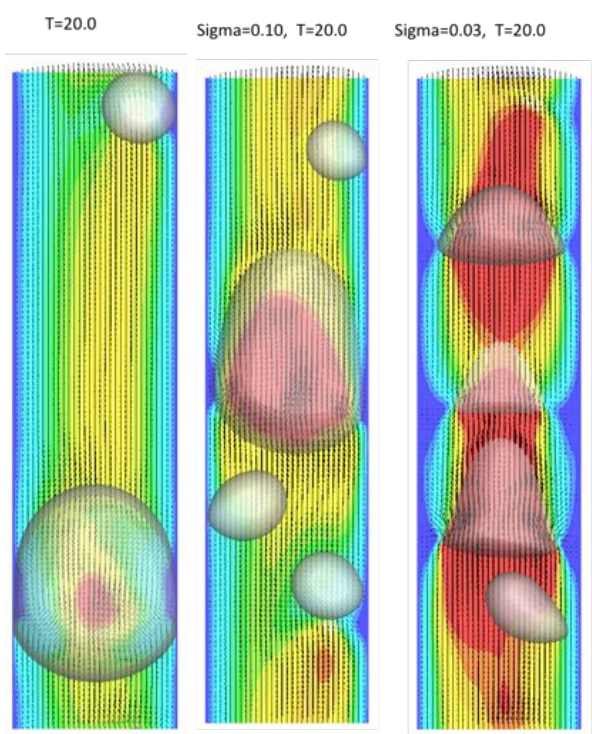

Figure 24. The dependency of the coalescence process on surface tension. The surface tension is highest on the left.

We have explored the evolution for several different surface tension coefficients and in figure 24 we show the interface and the streamwise velocity in a plane through the center of the domain for three simulations with different surface tension. The surface tension is highest in the frame on the left and lowest on the right. We have also gathered several quantitative measures of the flow, including total flow rate, wall shear, fluctuations, surface area and the different components of the surface area tensor (projections of the area along the different coordinate axis). In figure 25 we show two examples for three simulations with different surface tension. In the top frame the average velocity of the mixture is plotted

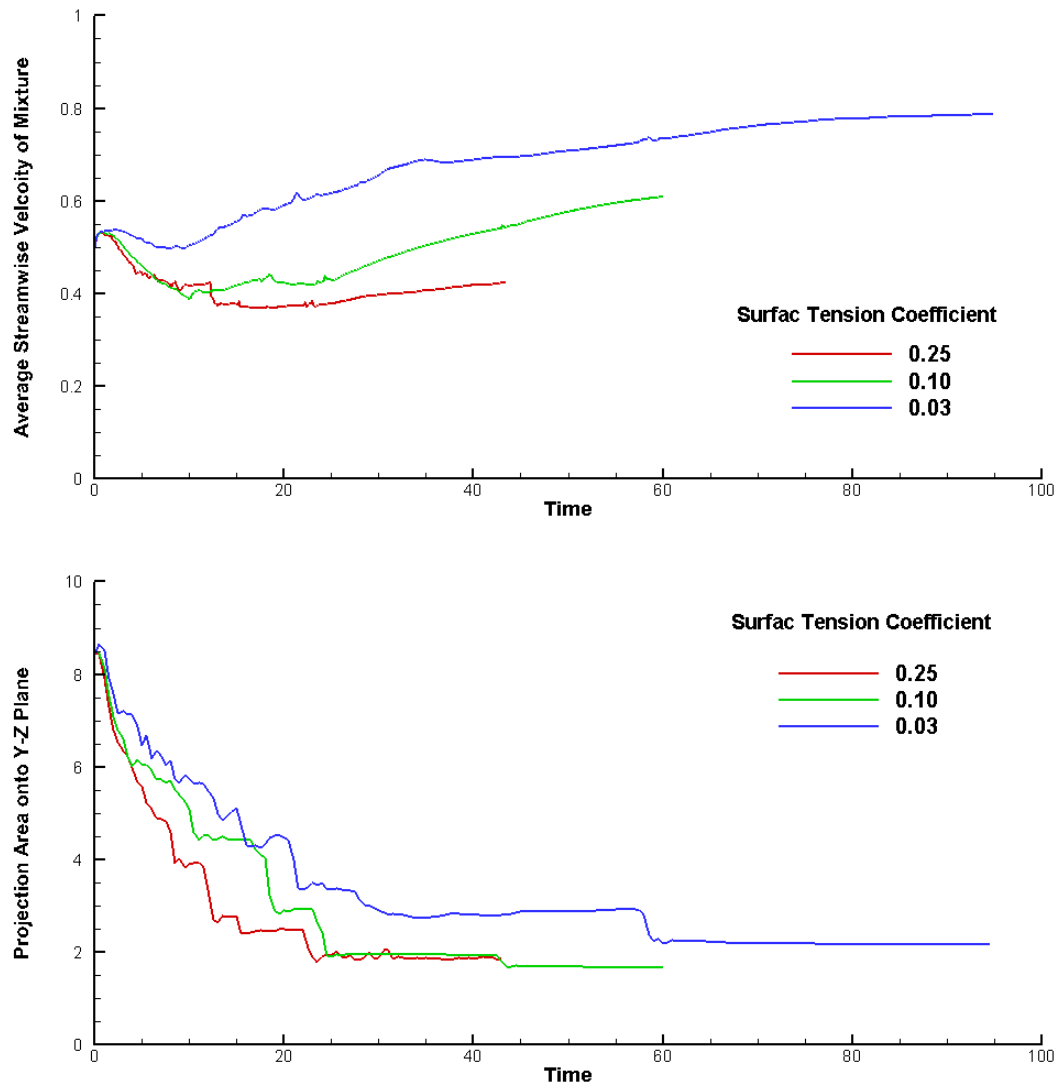

Figure 25. The average velocity of the mixture versus time for three runs with different surface tension (top) and the projection of the surface area in the streamwise direction versus time.

versus time for the three runs and it is not surprising that the velocity is highest for the lowest surface tension case, where the bubbles are most compliant. In the bottom frame we show the projection of the surface area in the streamwise direction. As the bubbles coalesce, their total surface area decreases rapidly and approaches twice the cross sectional area of the channel, as we would expect for a bubble that almost fills the channel. Notice that the high surface tension bubbles coalesce most rapidly and that the simulations were terminated once all the bubbles had coalesced into one.

We have also started to examine how sensitive the overall flow evolution is to exactly how the coalescence takes place. Figure 26 shows the evolution of the wall-shear (top) and the projection of the surface area in the streamwise direction. In one cases we coalesce the interfaces when they are about a grid spacing apart (red line) and in the other run we coalesce when the interfaces are two grid spaces

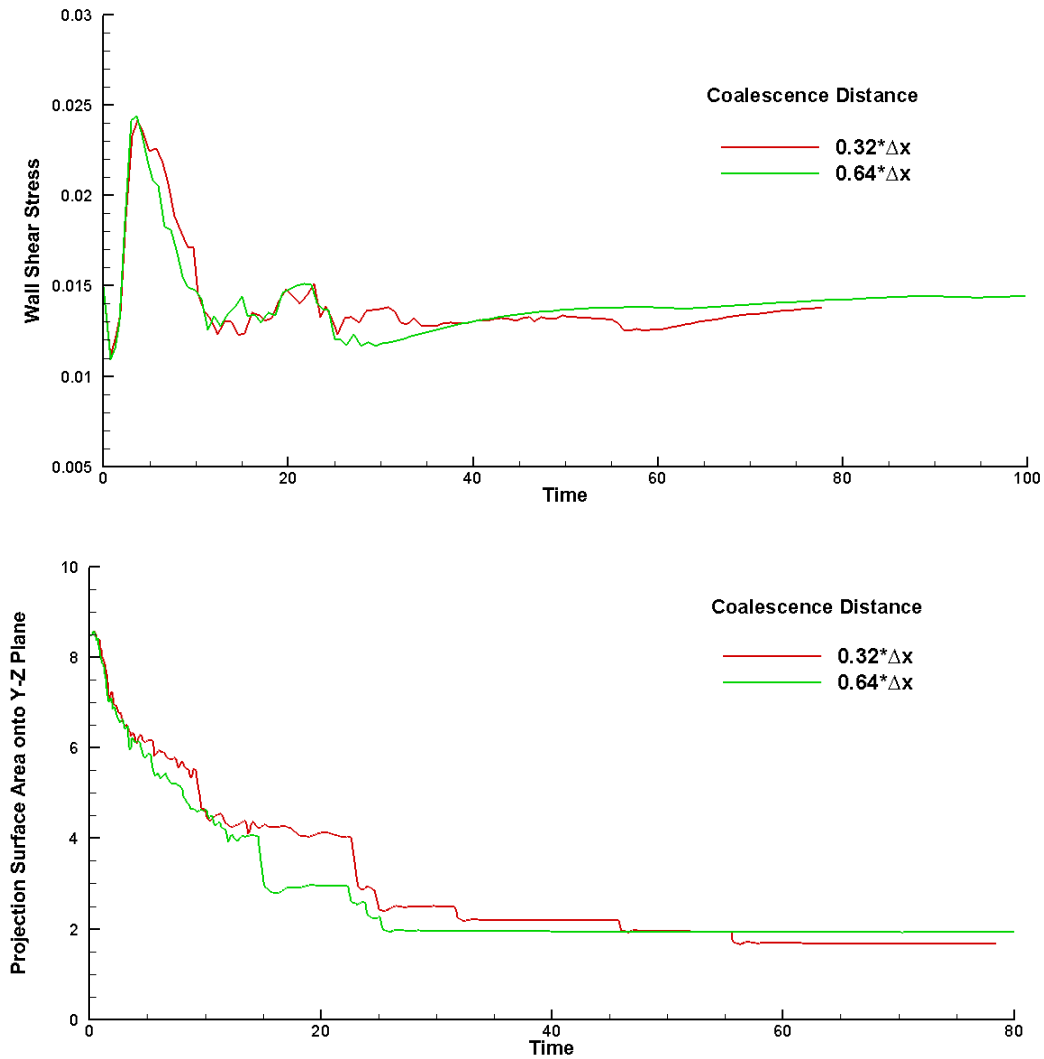

Figure 26. The wall shear (top) and the projection of the surface area in the streamwise direction versus time for two different coalescence criteria.

apart (green line). The overall evolution is clearly similar, although around time 20 it is clear that the bubbles with the larger criteria coalesce earlier than the ones that have to get closer before they merge.

4. Future Work

The results shown here, and our earlier results for the lift and drag on single bubbles have lead to significant new data and insight into bubbly flows. The early results have been published and the more recent results have been presented at several conferences and are being written up for submission to journals. We expect future work to focus on two thrust areas:

- Mining of the results from very large simulations of complex flows to help with the development of LES-like models (supports L1: 4, 11). Data obtained by averaging over the homogeneous directions and well as local filtering will be collected and we will explore the relations between unknown closure terms and quantities that are evolved in large-eddy and two-fluid simulations, using linear and nonlinear data reduction techniques (such as regression and neural networks, or more advanced techniques).
- Simulations of high void fraction flows where topology changes are an important part of the dynamics, and examination of how to use the results for modeling of such flows (supports L1: 15). The tasks include obtaining a better understanding of the importance of how the coalescence is modeled, including turbulence, and apply data analysis methods to extract information for modeling of the average or large scale flows.

While several other directions are possible for DNS of multiphase flows, such as further development for boiling flows, inclusion of surfactants, and mass transfer, we believe that the two listed above are both the most urgent ones, as well as those with the largest immediate impact.

Refrences

E. Labourasse, D. Lacanette, A. Toutant, P. Lubin, S. Vincent, O. Lebaigue, J.-P. Caltagirone, P. Sagaut. Towards large eddy simulation of isothermal two-phase flows: Governing equations and a priori tests. International Journal of Multiphase Flow 33 (2007) 1—39

A. Toutant, E. Labourasse, O. Lebaigue, and O. Simonin. DNS of the interaction between a deformable buoyant bubble and spatially decaying turbulence: a priori tests for LES two-phase flow modelling. Comp. Fluids 37 (7), 2008, 877—886.

S. Vincent, J. Larocque, D. Lacanette, A. Toutant, S. Lubin, and P. Sagaut. Numerical simulations of phase separation and a priori two-phase LES filtering. Comput. Fluids 37 (7), 2008, 898–906.

A. Toutant, M. Chandesris, D. Jamet, and O. Lebaigue. Jump conditions for filtered quantities at an under-resolved interface. Part 1: Theoretical developments. Int. J. Multiphase Flow 35 (12), 2009, 1100—1118.

A. Toutant, M. Chandesris, D. Jamet, and O. Lebaigue. b. Jump conditions for filtered quantities at an under-resolved interface. Part 2: A priori tests. Int. J. Multiphase Flow 35 (12), 2009, 1119—1129.

P. Trontin, S. Vincent, J. Estivalezes, and J. Caltagirone. Direct numerical simulation of a freely decaying turbulent interfacial flow. International. Journal of Multiphase Flow 36 (11—12), (2010), 891—907.

D. Jamet, O. Lebaigue, C. Morel, B. Arcen. Towards a multi-scale approach of two-phase flow modeling in the context of DNB modeling. Nuclear Engineering and Design 240 (2010) 2131—2138

Appendix

FTC3D is a specialized code for direct numerical simulations of multiphase flows. The "one-fluid" Navier-Stokes equations for incompressible flows, where a single set of equations is used for the whole flow domain, are solved on a regular structured staggered grid using an explicit projection method. Time integration is done by a second order predictor-corrector method, the viscous terms are discretized by second-order centered differences and the advection terms are approximated using a QUICK scheme. The pressure equation is solved using a multigrid method or a Krylov scheme (BIGSTAB).

The interface between the different fluids is tracked by connected marker points that are advected with the flow. The interface, or the "front," consists of points and triangular elements that connect the points. Once the marker points have been advected, a marker function is constructed from the new interface location. The front is also used to compute surface tension, which is then smoothed onto the fluid grid and added to the discrete Navier-Stokes equations. In addition to the computation of the surface tension and the construction of the marker function, the chief challenge in front-tracking is the dynamic updating of the front, whereby marker points are added or deleted to maintain the point density needed to fully resolve the interface. This is done fully automatically as part of the front advection.

The method was introduced by Unverdi & Tryggvason (1992) and for description of the original method, as well as various improvements and refinements, see Tryggvason et al. (2001) and Tryggvason et al. (2011). The method has been used to simulate a large range of multiphase flows, including bubbly flows. See, Bunner & Tryggvason (2002a,b), Esmaeeli & Tryggvason (2005), and Biswas, Esmaeeli & Tryggvason (2005), for example. For other implementation of similar ideas and applications to bubbly flows, see Dijkhuizen et al. (2010a,b); van Sint Annaland et al. (2006); Hao & Prosperetti (2004); Hua & Lou (2007); Muradoglu & Kayaalp (2006), for example.

References for Appendix:

Biswas, S., Esmaeeli, A. & Tryggvason, G. 2005 Comparison of results from DNS of bubbly flows with a two-fluid model for two-dimensional laminar flows. Int. J. Multiphase Flows 31, 1036–1048.

Bunner, B. & Tryggvason, G. 2002a Dynamics of homogeneous bubbly flows. Part 1. Rise velocity and microstructure of the bubbles. J. Fluid Mech. 466, 17–52.

Bunner, B. & Tryggvason, G. 2002b Dynamics of homogeneous bubbly flows. Part 2. Velocity fluctuations. J. Fluid Mech. 466, 53–84.

Bunner, B. & Tryggvason, G. 2003 Effect of bubble deformation on the stability and prop- erties of bubbly flows. J. Fluid Mech. 495, 77–118.

Esmaeeli, A. & Tryggvason, G. 2005 A direct numerical simulation study of the buoyant rise of bubbles at O(100) Reynolds number. Phys. Fluids 17, 093303.

Dijkhuizen, W., Roghair, I., Annaland, M. Van Sint & Kuipers, J. 2010a DNS of gas bubbles behaviour using an improved 3d front tracking model–drag force on isolated bubbles and comparison with experiments. Chem. Eng. Sci. 65, 1415–1426.

Dijkhuizen, W., Roghair, I., Annaland, M. Van Sint & Kuipers, J. 2010b DNS of gas bubbles behaviour using an improved 3d front tracking model–model development. Chem. Eng. Sci. 65, 1427–1437.

Hao, Y. & Prosperetti, A. 2004 A numerical method for three-dimensional gas–liquid flow computations. J. Comput. Phys. 196, 126–144.

Hua, J. & Lou, J. 2007 Numerical simulation of bubble rising in viscous liquid. J. Comput. Phys. 222, 769–795.

Muradoglu, M. & Kayaalp, A. D. 2006 An auxiliary grid method for computations of multiphase flows in complex geometries. J. Comput. Phys. 214, 858–877.

Tryggvason, G., Bunner, B., Esmaeeli, A., Juric, D., Al-Rawahi, N., Tauber, W., Han, J., Nas, S. & Jan, Y.-J. 2001 A front tracking method for the computations of multiphase flow. J. Comput. Phys. 169, 708–759.

Tryggvason, G., Scardovelli, R. & Zaleski 2011 Direct Numerical Simulations of Gas- Liquid Multiphase Flow. Cambridge University Press.

Unverdi, S. O. & Tryggvason, G. 1992 A front-tracking method for viscous, incompressible, multi-fluid flows. J. Comput. Phys. 100, 25–37.

van Sint Annaland, M., Dijkhuizen, W., Deen, N.G. & Kuipers, J.A.M. 2006 Numerical simulation of gas bubbles behaviour using a 3D front tracking method. AIChE J. 52, 99–110.